The relation between monogenetic and polygenetic dacitic volcanism. Case study from Tapias dome (<95 ka) and Cerro Machín volcano (<50 ka), Colombia

Jonathan Ortiz[1] ; **Jhoan Sebastián García[1]** ; **Hugo Murcia[2,3]** ;
Dayana Schonwalder-Ángel[4*] ; **Laura Sánchez-Torres[3]**

[1]Programa de Geología, Universidad de Caldas, Manizales, Colombia. gerencia.andina@hotmail.com; sebasgarcia0932@gmail.com
[2]Departamento de Ciencias Geológicas, Universidad de Caldas, Manizales, Colombia. hugo.murcia@ucaldas.edu.co
[3]Instituto de Investigaciones en Estratigrafía, Universidad de Caldas, Manizales, Colombia. lsancheztorres15@gmail.com
[4]Grupo de Investigación en Estratigrafía y Vulcanología (GIEV) Cumanday, Universidad de Caldas, Manizales, Colombia. (*) schonwalderd@gmail.com

Abstract

The Tapias lava dome is located ~5 km SE of the explosive, Cerro Machín polygenetic volcano, both located on the Colombian Central Cordillera. The edifices have been interpreted as generated by the same magmatic system; however, the genetic and temporal relations between both edifices have not been established. In this work, the Tapias dome is studied using petrographic characterizations, mineral-, whole-rock- and isotopic chemistry, geothermobarometric calculations, and a K/Ar radiogenic age, and subsequently it is explored the relationship with the Cerro Machín. The rocks from Tapias dome are porphyritic with phenocrysts of plagioclase (An_{28-48}), amphibole (tschermakite and magnesiohastingsite), biotite, quartz, and Fe-Ti oxides, embedded in a glassy groundmass. Petrographically, two types of amphibole crystals were recognized: type I, which is homogeneous, and type II, which displays different rims. The composition of Tapias is dacitic (SiO_2: 66.59 wt.%) with calc-alkaline affinity. Our geothermobarometric calculations indicate that type I amphibole crystallized at 871-874°C, between 10.2 and 10.4 km depth. The core of the type II amphibole crystallized at 852-920°C, between 8.5 and 12.3 km depth, while its rim did it at higher temperatures (880-973°C), but at similar depths (9.1-11.8 km). The K/Ar radiogenic age obtained for the groundmass shows an emplacement age not older than 95 ± 0.05 ka. When comparing the results to the Cerro Machín, it is noted that the mineral and compositional characteristics are nearly identical. These results suggest that indeed both volcanoes share the same magmatic system and are fed by magma hosted between ~9 and ~12 km depth. Moreover, it is proposed that the vent location of both edifices, as well as the time gap between the eruption at Tapias and the beginning of the activity at the Cerro Machín (~50 ka), are the result of crustal deformation caused by the interaction between the Otú-Pericos and Ibagué faults.

Keywords: Monogenetic volcanism; Magma differentiation; Local tectonics; Colombian Andes.

Relación entre vulcanismo dacítico monogenético y poligenético. Caso de estudio del domo Tapias (<95 ka) y volcán Cerro Machín (<50 ka), Colombia

Resumen

El domo Tapias es un edificio volcánico que se localiza ~5 km al SE del volcán poligenético explosivo Cerro Machín, ambos localizados en la Cordillera Central colombiana. La formación de estos volcanes ha sido interpretada a partir del mismo sistema magmático; sin embargo, la relación genética y temporal entre ellos no ha sido definida. En este trabajo, se analiza el domo Tapias a partir de petrografía, química mineral, química de roca total, isótopos, cálculos geotermobarométricos y una datación K/Ar, y posteriormente se explora la relación con el volcán Cerro Machín. Las rocas del domo Tapias son porfiríticas con fenocristales de plagioclasa (An_{28-48}), anfíbol (tschermakita y magnesiohastingsita), biotita, cuarzo y óxidos de Fe-Ti, embebidos en una masa fundamental vítrea. Petrográficamente, se reconocen dos tipos de anfíbol: el tipo I, con apariencia homogénea, y el tipo II, con bordes diferentes. La composición de Tapias es dacítica (SiO_2: 66,59 wt.%) de afinidad calco-alcalina. Los cálculos geotermobarométricos indican que: 1) los anfíboles tipo I cristalizaron a 871-874°C, entre 10,2 y 10,4 km de profundidad, y 2) los núcleos de los anfíboles tipo II cristalizaron a 852-920°C, entre 8,5 y 12,3 km de profundidad, mientras que los bordes, a temperaturas más altas (880-973°C), pero a profundidades similares (9,1-11,8 km). La edad K/Ar indica un emplazamiento no más antiguo que 95 ± 0,05 ka. Al comparar estos resultados con los reportados para el Cerro Machín, se observan unas características minerales y composicionales muy similares. Estos resultados sugieren que ambos volcanes son alimentados por el mismo magma hospedado entre ~9 y ~12 km de profundidad. Asimismo, se propone que el centro de emisión, así como el tiempo entre el emplazamiento de Tapias y el inicio de la actividad del Cerro Machín (~50 ka) son el resultado de deformación cortical relacionada con la interacción entre las fallas Otú-Pericos e Ibagué.

Palabras clave: Vulcanismo monogenético; Diferenciación magmática; Tectónica local; Andes colombianos.

Introduction

Evolved (andesite to rhyolite) rocks erupted from monogenetic volcanoes have been recognized in all tectonic settings (Németh *et al*., 2003) and it is described as low-volume (<1 km³) effusive eruptions that occur in a single event or multiple discontinuous pulses in a short period (less than a decade) (Connor and Conway, 2000; Németh, 2010; Kereszturi and Németh, 2012). Such eruptions are fed by dikes whose propagation are perpendicular to the minimum compressional stress (σ_3), which is oriented horizontally (Maccaferri *et al*., 2011). They can form volcanic fields (Németh, 2010; Cañón-Tapia, 2016), where its petrogenesis is explained as individual and spatially separated dikes fed by a common magma supply or reservoir at depth (Smith and Németh, 2017). In this case, evolved compositions are the results of fractionation, mixing and magma contamination processes, that occur due to relatively long residence time during the ascent to the surface (Murcia and Németh, 2020). Evolved monogenetic volcanoes, also occur in the vicinity of polygenetic volcanoes (Torres-Orozco *et al*., 2017), which are characterized by a complex magma-feeding system with one or more magma reservoirs and a network of dikes and sills (Cashman and Sparks, 2013). This complexity imposes further constraints on the propagation of dikes

to the surface, given the variations of the local stress caused by the reservoirs, dikes, and sills (Gudmundsson, 2006; Pansino and Taisne, 2019). Further constraints are expected in the presence of local and regional tectonic structures, as they can modify the state of stress at the crust, which in turn can favor or hinder the propagation of dikes to the surface (van Wyk de Vries and Merle, 1998; Valentine and Krogh, 2006).

In the central part of the Colombian Central Cordillera (Figure 1A) is located the Tapias dome (4.467706, -75.363457, 2525 masl), a monogenetic volcano situated ~5 km SE of the Holocene Cerro Machín composite volcano (4.486817, -75.386178, 2750 masl; Figure 1B and 1C). Both volcanoes are built over Permo-Triasic to Jurassic rocks from the Cajamarca Complex, characterized by a package of orthogneiss, phyllites, quartzites, greenschist, and graphite schists (Vargas *et al*., 2005; Villagómez *et al*., 2011; Blanco-Quintero *et al*., 2014). They form the southernmost expression of volcanism in the San Diego – Cerro Machín Volcano-Tectonic Province (SCVTP) (Figure 1B). The Tapias dome has a diameter of 1.3 km, a height of 500 m, and an area of ~1.29 km². On the other hand, the Cerro Machín has a 2.4 km open-crater and an intra-crater dome that stands 490 m in height (Piedrahita *et al*., 2018). The eruptive history of this volcano is well-

known (Méndez-Fajury, 1989; Cepeda *et al.*, 1995; Thouret *et al.*, 1995; Rueda, 2005; Murcia *et al.*, 2010), which is characterized by producing dacitic Plinian and Vulcanian eruptions, with the first one occurring 47,000 years BP (Méndez, 2001) and the last one only around 900 years BP (Rueda, 2005; Laeger *et al.*, 2013; Piedrahita *et al.*, 2018). The area is influenced by two main dextral strike-slip fault systems (Figure 1C), the Otú-Pericos (NE) fault to the East and the Ibagué (ENE) fault to the Southeast (Osorio *et al.*, 2008; Rozo-Gómez, 2012; Gómez-Díaz and Mariño-Arias, 2020).

In this work, we characterize the Tapias dome through new petrography, mineral and isotopic chemistry, and a K/Ar radiogenic age, together with published whole-rock chemistry. Then, we present geothermobarometric calculations and compare the results with available data from the Cerro Machín volcano. This allowed us to show the link between both volcanic edifices. Finally, we evaluate the volcanism from a tectonic context to provide insights into the interplay between tectonics and magmatism in the area.
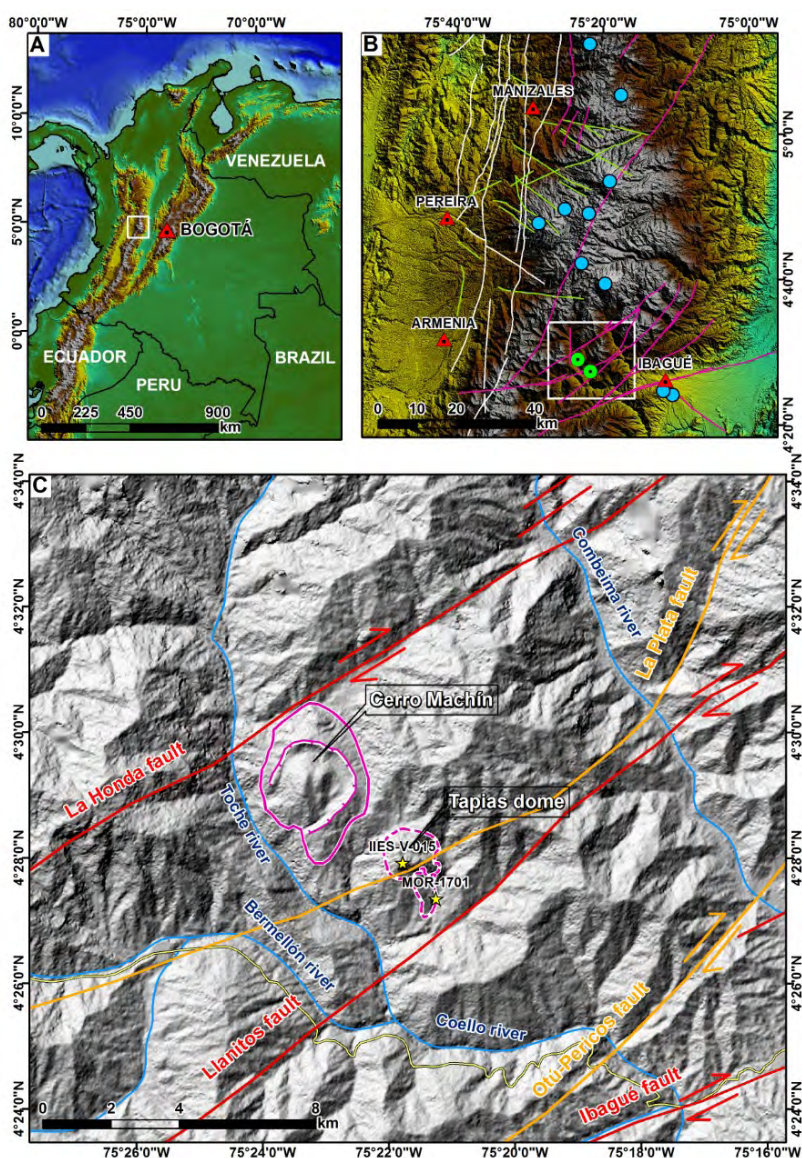
Figure 1. Localization map. **A.** Physical map of Colombia, white square marks the area of the San Diego - Cerro Machín Volcano-Tectonic Province (SMVTP), located on the central part of the Central Cordillera. **B.** Detailed map of the SMVTP, blue circles mark the location of the main volcanoes of the province. White lines mark reverse faults, pink lines mark strike-slip faults and green lines mark normal faults. The area of Cerro Machín volcano and Tapias dome is identified with a quite square. **C.** DEM of the study area. Faults marked in red are part of the Ibagué fault system. Faults marked in orange are part of the Otú-Pericos fault, the fault traces are taken from Cuéllar-Cárdenas *et al.* (2014).

Geologic framework

The Plio-Quaternary SCVTP (Figure 1) is a 140 km long magmatic-tectonic segment, located in the axis of the Central Cordillera, in the northernmost part of the Colombian volcanic arc (Martínez *et al*., 2014). It is the result of the eastern oblique subduction of the Nazca plate below the South American plate, and the collision of the Panamá-Chocó Block (van der Hilst and Mann, 1994; Jaramillo *et al*., 2019; Mora-Páez *et al*., 2019). Currently, the SCVTP is located ~280 km from the trench, with crustal thickness reaching up to 52 km below the Cerro Machín (Yarce *et al*., 2014; Poveda *et al*., 2015, 2018). At a regional scale, three main types of fault systems have been recognized in the SCVTP (Figure 1B). To the west of the Central Cordillera, a group of N-S reverse faults such as the Cauca-Almaguer, Silvia-Pijao, and San Jeronimo (Maya and Gonzalez, 1995) are identified. Across the Central Cordillera, representing regional shear zones, there are the NE-trending right-lateral strike-slip faults such as the Palestina, Ibagué, and Otú-Pericos (Paris *et al*., 2000; Osorio *et al.*, 2008; Gómez-Díaz and Mariño-Arias, 2020). Towards the middle part of the SCVTP, a group of normal faults such as the Villamaria-Termales (NW-SE) and Santa Rosa (N70E) is present (Thouret *et al*., 1990; Bohórquez *et al*., 2005; Mejía-Toro, 2012). This tectonic framework and the systematic inversion of double couple focal mechanisms of shallow earthquakes in the area allowed Cortés *et al*. (2005) to determine a compressive stress tensor where the principal stress (σ_1) is oriented NW-SE within a predominantly strike-slip regime.

Cerro Machín is a Holocene polygenetic volcano whose current edifice was formed from successive Plinian and Vulcanian eruptions (at least six eruptions during the last 5000 years), with magmatic and phreatomagmatic deposits (Rueda, 2005; Piedrahita *et al.*, 2018). Within the products of the volcano, it has been recognized a lava dome (the most recent eruption 900 B.P.) (Laeger *et al*., 2013; Piedrahita *et al.*, 2018) and PDCs of consistent dacitic composition (59.01-65.99 wt. % SiO_2) (Rueda, 2005; Laeger *et al.*, 2013; Errázuriz-Henao *et al*., 2019). On the other hand, the Tapias dome has not been previously studied, appearing only in the cartography of the area (without any compositional data) defined as an andesitic dome (Mosquera *et al*., 1982).

From a tectonic context, two main models have been proposed to explain the emplacement of Cerro Machín.

Initially, Mosquera *et al*. (1982) and Cepeda *et al*. (1995) proposed that the volcano was emplaced in the intersection of the Cajamarca and Machín faults (see Figure 1 in Piedrahita *et al., 2018*). However, neither the work of Mosquera *et al*. (1982) nor Cepeda *et al*. (1995) clearly describes the location of the Machín fault. In addition, no evidence for the Machín fault using remote sensing studies on the area was observed (Gómez-Díaz and Mariño-Arias, 2020). Another model was proposed by Rueda (2005), explaining the volcano's emplacement as the result of a pull-apart structure generated by transcurrent faults (Cajamarca and Salento) with lateral displacement and a high deep angle. Yet, neither of these models explains the emplacement of the Tapias dome and does not take into consideration the two major tectonic systems in the area, which are the right-lateral strike-slip faults Otú-Pericos (NE) and Ibagué (ENE/70° NW), both crossing each other obliquely SE from Cerro Machín and Tapias, which generates a zone of tectonic stress accumulation (Bohórquez *et al*., 2005; Montes *et al*., 2005). These faults represent transversal shear zones in the Central Cordillera (Diederix *et al*., 2006), and accommodate the deformation by developing associated minor synthetic and antithetic faults (Peacock and Sanderson, 1996; Martel, 1997; Kim *et al*., 2004). In the study area, these faults are recognized as La Plata fault for the Otú-Pericos system, and El Filtro, La Honda, and Llanitos, among others, for the Ibagué system (Figure 1C), as mapped by Cuéllar-Cárdenas *et al.* (2014).

Methodology

In this work, we present data from two samples from Tapias dome. The Sample IIES–V–O15 (4°27'55.04" N, 75°21'47.43" W, 2160 masl; Figure 1C) was collected by us during a field campaign in 2019. During fieldwork, we follow the mapping of the dome performed by Mosquera *et al*. (1982) to find outcrops of fresh rock, from which we collected one rock without noticeable alterations. The sample IIES-V-015 was used for petrographic and mineral chemistry analyses, as well that for radiogenic K/Ar dating. The sample MOR-1701 (4°27'20.97" N, 75°21'15.77" W; Figure 1C) was initially reported in the supplementary material of Errázuriz-Henao *et al.* (2019) as part of Cerro Machín, but it was collected at Tapias dome. From this sample, we use the whole-rock geochemistry data published by Errázuriz-Henao *et al.* (2019) and present new isotopic data.

Petrography

A thin section from sample IIES-V-015 was made in the Teclab laboratories (Colombia) and their polishing and the application of conductive carbon coating (15 nm) was done at the sample preparation laboratory in the Earth Observatory of Singapore. Conventional petrographic descriptions and point counting (646 in total) were performed, using a Nikon Eclipse 50i microscope from the Mineral Deposits Laboratory at Universidad de Caldas, Colombia. Following González (2008), we defined phenocrysts (>0.5 mm), microphenocrysts (0.5 – 0.05 mm), and microlites (<0.05 mm). The groundmass was defined by glass and microlites.

Mineral and Isotopic chemistry

We performed in situ quantitative analysis (45) in plagioclase, amphibole, and biotite phenocrysts and microphenocrysts, using a JXA-8530F Field Emission Electron Probe X-ray Micro-Analyser (FE-EPMA) equipped with 5 wavelength-dispersive spectrometers, at the Facility for Analysis, Characterization, Testing, and Simulation (FACTS) in Nanyang Technological University (NTU), Singapore. Point analyses were acquired using a focused beam at a probe current of 20 nA and an accelerating voltage of 15 kV. The current was reduced to 10 nA and a defocused beam diameter of 3 was used for the analysis of plagioclase, to reduce beam dosage and resultant sodium signal decay. Results were quantified using well-characterized natural and synthetic external calibration standards and a ZAF matrix correction procedure. Oxygen content was assumed from cation abundance, with all iron present as Fe^{2+}. Error on repeat analysis of standard reference materials was <1% of measured values. Kα X-ray lines were monitored for 20 – 60 s for each element, depending on expected concentrations except for Na Kα which was monitored for only 10 s. Background measurements were performed on either side of each peak position for combined counting times equaling the corresponding peak counting times. Measured peak and background positions were found to be free of interferences within the sample and standard matrices. The obtained results were processed and classified using the GCDkit 4,1 (Janoušek *et al*., 2006), CFU, and CFU-PINGU software (Cortés, 2022). To determine the type of amphibole present we used the Leake *et al*. (1997) classification, which uses cations per formula unit for the amphibole equation $AB_2 C_5 T_8 O_{22} (OH)_2$. Some plagioclase and biotite analyses show low values of total oxides; however, these were used with caution. The methodology for isotopic analysis is described in Errázuriz-Henao *et al*. (2019).

Radiometric K/Ar dating

Fresh glassy groundmass fragments (<1 mm) from the collected sample were analyzed in ActLabs (Canada) using the following procedure: aliquots of the samples were weighted into an Al container, loaded into the sample system of extraction unit, degassed at ~100°C for two days to remove the surface gases. Argon was extracted from the sample in a double vacuum furnace at 1700°C. The determination of radiogenic argon content was carried out twice on an MI-1201 IG mass spectrometer by isotope dilution method with ^{38}Ar as a spike, which was introduced to the sample system before each extraction. The extracted gases were cleaned up in a two steps purification system. Then pure Ar was introduced into a custom-built magnetic sector mass spectrometer (Reynolds type). Two globally accepted standards (P-207 Muscovite and 1/65 "Asia" rhyolite matrix) were measured for ^{38}Ar spike calibration. For age calculations the international values of constants were used as follows: $\lambda K = 0.581 \times 10^{-10}$ y−1, $\lambda \beta\text{-} = 4.962 \times 10^{-10}$ y−1, $40K = 0.01167$ (at.%).

Results

Petrography

Macroscopically the Tapias dome displays a porphyritic texture with crystals of plagioclase, amphibole, and biotite (up to 1 cm in diameter), embedded in a glassy light grey groundmass. At a microscopic level, it is observed a prevalent porphyritic texture with subhedral – euhedral phenocrysts and microphenocrysts of plagioclase (0.1 – 2.5 mm, 27 vol.%), amphibole (0.2 – 2 mm, 16 vol.%), biotite (0.2 – 1.8 mm, 2 vol.%), within a glassy groundmass (51 vol.%) with microlites of plagioclase and amphibole (Figure 2). Microphenocrysts of anhedral quartz (up to 0.8 mm, 1 vol.%) and accessory euhedral Fe-Ti (<0.1 mm, 1 vol.%) oxides are also observed. Glomerocrysts of amphibole, plagioclase, and amphibole-biotite also appear, although they are scarce. Plagioclase phenocrysts (Figures 2A and 2B) display prismatic habit, inclusions of apatite and amphibole, and diverse zonation patterns: Carlsbad, albite-type, patchy, and oscillatory. A few plagioclase crystals also display well-marked rims (light grey), some of which show dissolution features. This is also observed in the light grey zone of plagioclase phenocrysts with Carlsbad twinning. Amphibole crystals (Figures 2C and 2D) appear as prismatic and tabular, some with plagioclase inclusions. Two main populations are recognized. Type I amphiboles are crystals without zonation of brown and olive-green colors, whereas type II amphiboles

are mostly brown with a marked yellowish rim. Both types of amphiboles are common as phenocrysts and microphenocrysts, although type II appears in relatively larger proportions than type I amphiboles. Biotite phenocrysts (Figure 2E) are characterized by

their laminar and tabular habit and brown coloration. Some of the phenocrysts display very narrow yellowish rims, and some also display apatite inclusions. Quartz microphenocrysts (Figure 2F) are rounded and sometimes fractured.
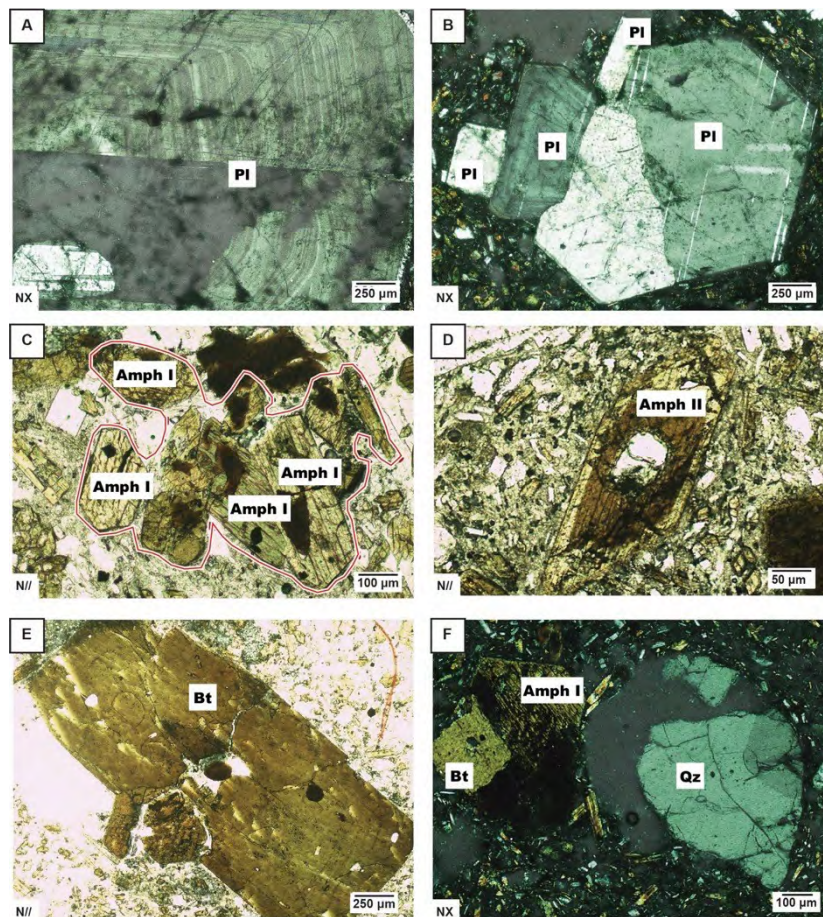
Figure 2. Photomicrographs from Tapias dome (sample IIES-V-015). **A.** Plagioclase (Pl) phenocryst with oscillatory zonation. **B.** Plagioclase glomerocrysts, with crystal displaying oscillatory and albite-type zonation. **C.** Glomerocrysts and phenocrysts of amphibole type I (Amph I) crystals. **D.** Amphibole type II (Amph II) phenocryst, displaying zonation on its rim. **E.** Biotite phenocryst. **F.** Phenocryst of quartz, amphibole type I and biotite.

Mineral chemistry

Table 1 shows the data for the in-situ analysis of the plagioclase, amphibole, and biotite phases. The plagioclase (Figure 3A) is classified as andesine (An_{28-48}), and its compositional range falls within the range displayed by-products of the Cerro Machín, which include rocks from the Plinian and Vulcanian eruptions, as well as rocks from the intra-crater dome (Laeger *et al.*, 2013; Regnier, 2015). Likewise, the Mg-rich composition of the biotite crystals (Figure 3B) (Foster, 1960) is observed in both volcanoes. Both amphibole populations observed in the petrography are considered calcic amphiboles (Leake *et al.*, 1997) and are classified as tschermakite and magnesiohastingsite

(Figure 3C), which are also the composition displayed by amphiboles from the explosive and effusive deposit of the Cerro Machín. To better constrain the compositional difference between the two types of amphiboles, we use a binary compositional diagram (Figure 3D), which shows that the composition of type I amphiboles is the same composition of the core from the type II (10.20 – 13.10 wt.% MgO). We also notice how the rim from the type II amphiboles is relatively richer in MgO (16.07 – 16.65 wt. %) and hence indicates an inverse zonation. The same behavior is observed in the amphiboles from the intra-crater dome of the Cerro Machín (Laeger *et al.*, 2013).

Table 1. Mineral analyses for the main mineral phases of Tapias dome (sample IIESV-015).

Mineral								Plagioclase							
Code	C9-b1	C9-b8	C9-b9	C10-a2	C10-a3	C10-a4	C10-a5	C10-a6	C10-a7	C10-a8	C10-a9	C10-a10	C10-a11	C10-a12	C10-a13
SiO_2	53.87	57.64	57.27	57.03	57.40	57.84	57.96	58.41	57.36	57.84	57.96	57.74	58.20	59.04	59.44
Al_2O_3	26.85	23.51	23.76	23.32	23.77	23.27	23.34	23.48	24.04	24.03	23.86	24.48	24.19	23.48	23.52
FeO	0.33	0.12	0.13	0.15	0.12	0.12	0.10	0.11	0.09	0.08	0.10	0.09	0.09	0.10	0.09
CaO	9.91	6.04	6.51	6.11	6.27	6.00	5.95	5.84	6.60	6.37	6.47	6.85	6.61	5.82	5.90
Na_2O	5.90	8.22	7.82	8.08	7.83	7.93	8.26	8.22	7.70	7.93	7.87	7.86	8.00	8.14	8.29
K_2O	0.20	0.43	0.40	0.44	0.41	0.42	0.44	0.43	0.38	0.39	0.37	0.36	0.38	0.44	0.43
Total	97.06	95.97	95.89	95.12	95.79	95.57	96.04	96.49	96.18	96.64	96.62	97.38	97.47	97.02	97.66
% An	47.59	28.17	30.80	28.73	29.97	28.80	27.76	27.52	31.45	30.08	30.57	31.86	30.70	27.60	27.54
Cations per formula unit (c.p.f.u.) based on 8 oxygens															
Si	2.51	2.69	2.67	2.68	2.68	2.70	2.70	2.70	2.67	2.67	2.68	2.65	2.67	2.71	2.72
Al	1.47	1.29	1.31	1.29	1.31	1.28	1.28	1.28	1.32	1.31	1.30	1.33	1.31	1.27	1.27
Fe^{2+}	0.01	0.00	0.00	0.01	0.00	0.00	0.00	0.00	0.00	0.00	0.00	0.00	0.00	0.00	0.00
Ca	0.49	0.30	0.33	0.31	0.31	0.30	0.30	0.29	0.33	0.32	0.32	0.34	0.33	0.29	0.29
Na	0.53	0.74	0.71	0.74	0.71	0.72	0.75	0.74	0.69	0.71	0.71	0.70	0.71	0.73	0.73
K	0.01	0.03	0.02	0.03	0.02	0.03	0.03	0.03	0.02	0.02	0.02	0.02	0.02	0.03	0.02

Mineral								Plagioclase					
Code	C10-a14	C10-a15	C11-a1	C11-a2	C11-a3	C11-a4	C11-a5	C11-a6	C11-a7	C11-a8	C11-a9	C11-a10	C13-a11
SiO_2	58.45	56.20	55.65	58.24	59.86	59.16	60.67	60.14	60.78	60.03	57.96	58.88	56.75
Al_2O_3	24.26	26.11	27.13	25.01	24.39	24.78	24.18	24.35	24.32	24.67	24.41	23.94	23.56
FeO	0.07	0.11	0.32	0.13	0.13	0.10	0.13	0.13	0.14	0.16	0.12	0.10	0.14
CaO	6.51	8.59	9.80	7.55	6.53	7.11	6.10	6.48	6.12	6.55	6.76	6.14	6.44
Na_2O	7.73	6.71	5.81	7.20	7.87	7.52	8.22	7.75	7.96	7.63	7.77	8.06	7.80
K_2O	0.37	0.27	0.21	0.39	0.44	0.38	0.45	0.40	0.43	0.38	0.39	0.44	0.42
Total	97.39	97.99	98.92	98.53	99.23	99.05	99.77	99.24	99.75	99.42	97.40	97.56	95.10
% An	31.08	40.80	47.65	35.89	30.67	33.58	28.35	30.90	29.10	31.49	31.76	28.88	30.60
Cations per formula unit (c.p.f.u.) based on 8 oxygens													
Si	2.68	2.58	2.53	2.64	2.69	2.67	2.71	2.70	2.71	2.69	2.66	2.69	2.67
Al	1.31	1.41	1.45	1.34	1.29	1.32	1.27	1.29	1.28	1.30	1.32	1.29	1.31
Fe^{2+}	0.00	0.00	0.01	0.01	0.00	0.00	0.00	0.00	0.01	0.01	0.00	0.00	0.01
Ca	0.32	0.42	0.48	0.37	0.31	0.34	0.29	0.31	0.29	0.31	0.33	0.30	0.32
Na	0.69	0.60	0.51	0.63	0.69	0.66	0.71	0.67	0.69	0.66	0.69	0.71	0.71

Continuation from Table 1.

Mineral	Amphibole														Biotite		
Code	C11-b1	C11-b2	C11-c1	C11-c2	C12-a1	C12-a2	C12-a3	C12-a4	C12-a5	C12-c0	C14-a2	C14-a4	C14-a5	C14-a7	C2-b	C6-a	C7-b
Type	I-core	I-core	II-rim	II-core	II-core	II-rim	II-core	II-core	II-rim	II-core	II-rim	II-core	II-core	II-rim			
SiO_2	42.26	42.06	42.78	42.66	41.34	42.87	40.77	43.77	43.54	42.14	42.82	42.98	41.55	43.70	30.13	33.39	32.00
TiO_2	1.33	1.34	2.44	1.28	1.41	2.05	1.90	1.21	2.15	1.21	2.54	1.25	1.29	2.06	3.52	3.77	3.49
Al_2O_3	10.93	11.04	10.69	10.28	11.14	10.58	11.68	9.98	10.05	10.33	10.88	11.08	10.38	10.59	13.02	14.06	14.75
FeO	16.63	16.77	8.53	17.08	16.95	10.30	17.00	13.86	8.81	16.83	8.90	16.27	16.91	9.37	18.33	19.15	17.89
MnO	0.36	0.40	0.11	0.40	0.41	0.17	0.40	0.35	0.13	0.43	0.11	0.42	0.43	0.13	0.17	0.20	0.16
MgO	10.90	10.67	16.35	10.86	10.54	15.23	10.20	13.10	16.65	11.05	16.07	11.02	11.06	16.22	11.79	11.66	11.02
CaO	10.87	11.01	11.00	11.14	11.08	11.02	10.74	10.72	10.67	11.10	11.07	10.93	11.05	11.01	-	-	-
Na_2O	2.06	2.08	2.46	1.98	2.05	2.35	2.33	2.11	2.50	1.96	2.51	1.99	2.06	2.43	0.67	0.53	0.64
K_2O	0.78	0.90	0.60	0.84	0.89	0.55	0.72	0.46	0.52	0.79	0.60	0.70	0.70	0.54	8.50	8.52	7.84
P_2O_5	0.01	0.01	0.06	0.03	0.03	0.04	0.03	0.01	0.02	0.00	0.03	0.01	0.02	0.04	-	-	-
Total	96.13	96.28	95.02	96.55	95.85	95.16	95.76	95.57	95.03	95.84	95.54	96.65	95.45	96.08	86.12	91.28	87.82
Cations per formula unit (c.p.f.u.) based on 13 cations															c.p.f.u. based on 22 oxygens		
^{T}Si	6.34	6.33	6.26	6.41	6.27	6.31	6.18	6.48	6.34	6.36	6.25	6.39	6.30	6.32	5.19	5.37	5.31
^{T}Al^{IV}	1.66	1.67	1.74	1.59	1.73	1.69	1.82	1.52	1.66	1.64	1.75	1.61	1.70	1.68	2.64	2.63	5.69
^{C}Al^{VI}	0.28	0.29	0.11	0.23	0.26	0.14	0.27	0.22	0.06	0.20	0.12	0.34	0.15	0.13	0.00	0.03	0.20
^{C}Ti	0.15	0.15	0.27	0.14	0.16	0.23	0.22	0.13	0.24	0.14	0.28	0.14	0.15	0.22	0.46	0.46	0.44
^{C}Fe^{3+}	0.83	0.74	0.80	0.73	0.76	0.82	0.78	0.94	0.98	0.85	0.76	0.79	0.91	0.89	-	-	-
^{C}Mg	2.44	2.39	3.57	2.43	2.38	3.34	2.31	2.89	3.61	2.49	3.50	2.44	2.50	3.50	3.03	2.80	2.73
^{C}Fe^{2+}	1.26	1.37	0.25	1.41	1.38	0.45	1.38	0.77	0.09	1.27	0.33	1.23	1.24	0.25	2.64	2.57	2.48
^{C}Mn	0.00	0.05	0.00	0.05	0.05	0.02	0.05	0.00	0.02	0.05	0.01	0.00	0.00	0.00	0.02	0.03	0.02
^{B}Ca	1.75	1.77	1.72	1.79	1.80	1.74	1.75	1.70	1.66	1.79	1.73	1.74	1.79	1.71	-	-	-
^{B}Na	0.25	0.23	0.28	0.21	0.20	0.26	0.25	0.30	0.34	0.21	0.27	0.26	0.21	0.29	-	-	-
^{A}Na	0.35	0.38	0.42	0.37	0.40	0.41	0.43	0.31	0.37	0.37	0.44	0.32	0.40	0.39	0.23	0.17	0.21
^{A}K	0.15	0.17	0.11	0.16	0.17	0.10	0.14	0.09	0.10	0.15	0.11	0.13	0.14	0.10	1.87	1.75	1.66

The superscript T, C, B and A indicate the element position in the amphibole crystal structure.
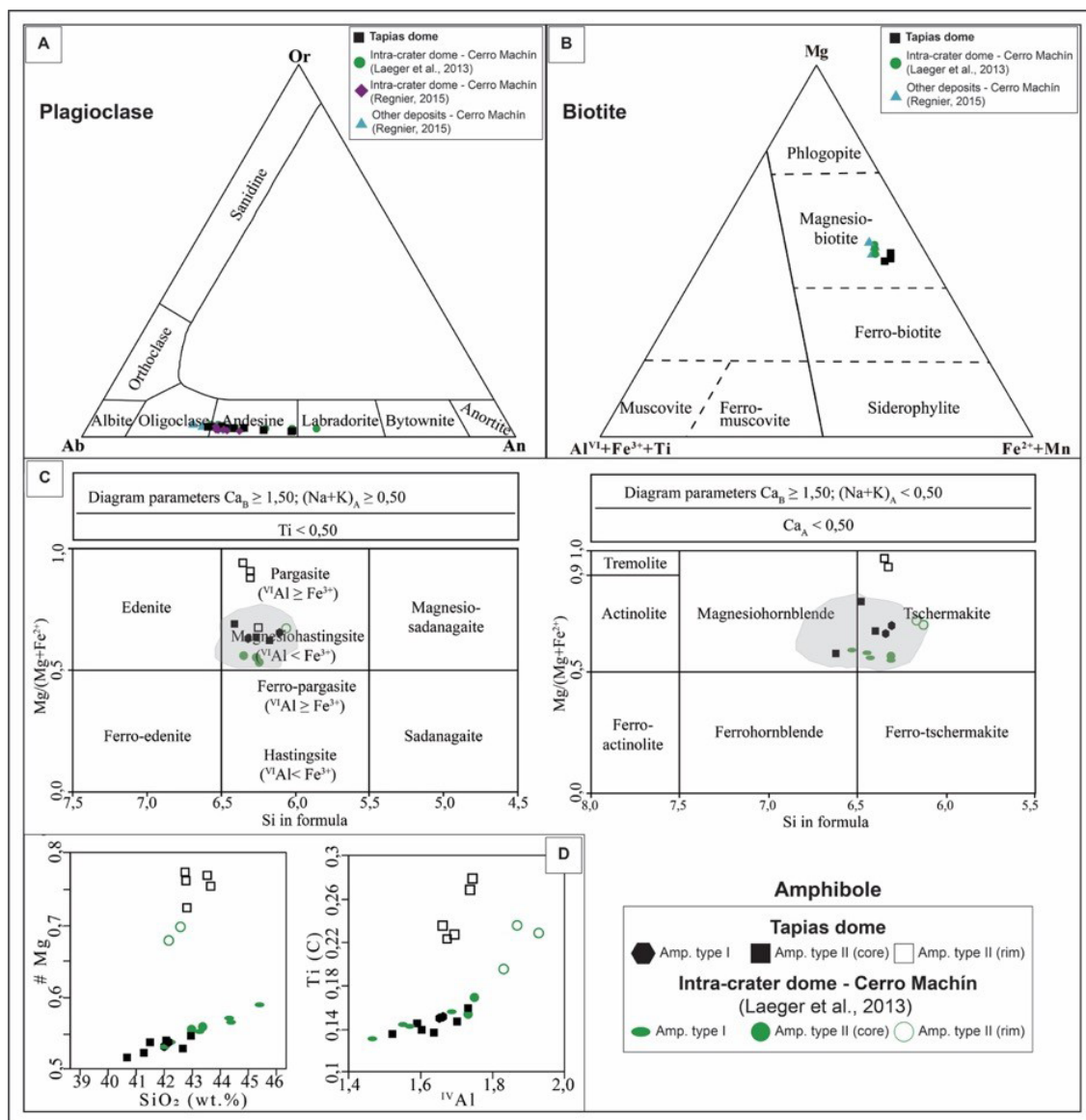
Figure 3. Classification of main mineral phases at Tapias dome (IIES-V-015) and Cerro Machín volcano (CMV). **A.** Plagioclase composition (Rahman and MacKenzie, 1969). **B.** Biotite classification (Foster, 1960). **C.** Amphibole classification (Leake *et al.*, 1997). **D.** Amphibole binary diagrams of SiO_2 *vs* #Mg and ^{IV}Al *vs* Ti(C).

Whole-rock chemistry and radiogenic isotopes

The concentration of major element oxides, trace elements, and radiogenic ratios are reported by Errázuriz-Henao *et al.* (2019) in their supplementary material (sample MOR-1701). For the same sample, in this work (Table 2) we report new isotopic data.

The Tapias dome is classified as dacitic with medium-K calc-alkaline affinity (66.59 wt. % SiO_2, 2.00 wt. % K_2O; Figure 4), which are within the compositions reported for products of the Cerro Machín that have a media of 65.04 wt. % SiO_2 and 2.12 wt. % K_2O (Cepeda *et al.*, 1995; Rueda, 2005; Laeger *et al.*, 2013; Regnier,

2015; Errázuriz-Henao *et al.*, 2019). To identify the geochemical characteristic of the magmatic source, we consider ratio-ratio plots of highly incompatible elements like Ba/Th *vs* Ba/Ce (Rollinson, 1993). Figure 5A shows that the Th/Ce ratio of the samples from both volcanoes seems to follow the same trend. Likewise, rocks from both volcanoes show similar patterns for other trace elements (Figures 5B and 5C); at the REE diagram normalized to chondrite, the rocks display relative enrichment of the LREE compared with the HREE ((La/Sm)$_N$ = 2.9 – 4.3; (Gd/Yb)$_N$ = 2.3 – 2.9), whereas the incompatible multi-elements diagram shows decoupling between LILE and HFS

elements, with LILE being enriched compared to N-MORB. The rocks also show positive anomalies of Ba, Pb, Sr, and Nd (on a smaller scale), pronounced negative anomalies of Nb, Ta, and P, and minor anomalies of Ti. Eu/Eu* varies between 0.87 and 0.93.

Figure 6 shows the radiogenic isotopes ratios of the Tapias dome compared to data from the Cajamarca Complex (Cavell, 2020) and the Cerro Machín, Santa Isabel, Santa Rosa, and volcanoes (Errázuriz-Henao *et al.*, 2019; Cavell, 2020). To the best of our knowledge, are the closest volcanoes (~25, 34 – 37 km) with known isotopic data. It can be observed how rocks from both Tapias and Cerro Machín plot close to each other and are distinctively different from Nevado del Tolima, Santa Rosa and Santa Isabel volcanoes. Tapias dome

shows a higher ratio of both $^{143}Nd/^{144}Nd$ and $^{176}Hf/^{177}Hf$ when compared to Cerro Machín, whereas the latter shows a higher $^{87}Sr/^{86}Sr$ ratio (Figures 6A and 6B). The inset in both figures shows the isotopic ratios for the Cajamarca Complex (Cavell, 2020), which have noticeably higher ratios of $^{87}Sr/^{86}Sr$ compared to the volcanoes in the area.

Table 2. Isotopic compositions sample MOR-1701.

Isotope	Value
$^{87}Sr/^{86}Sr$	0.704907
$^{206}Pb/^{204}Pb$	18.960178
$^{207}Pb/^{204}Pb$	15.643066
$^{208}Pb/^{204}Pb$	38.787379
$^{143}Nd/^{144}Nd$	0.512712
$^{176}Hf/^{177}Hf$	0.282906
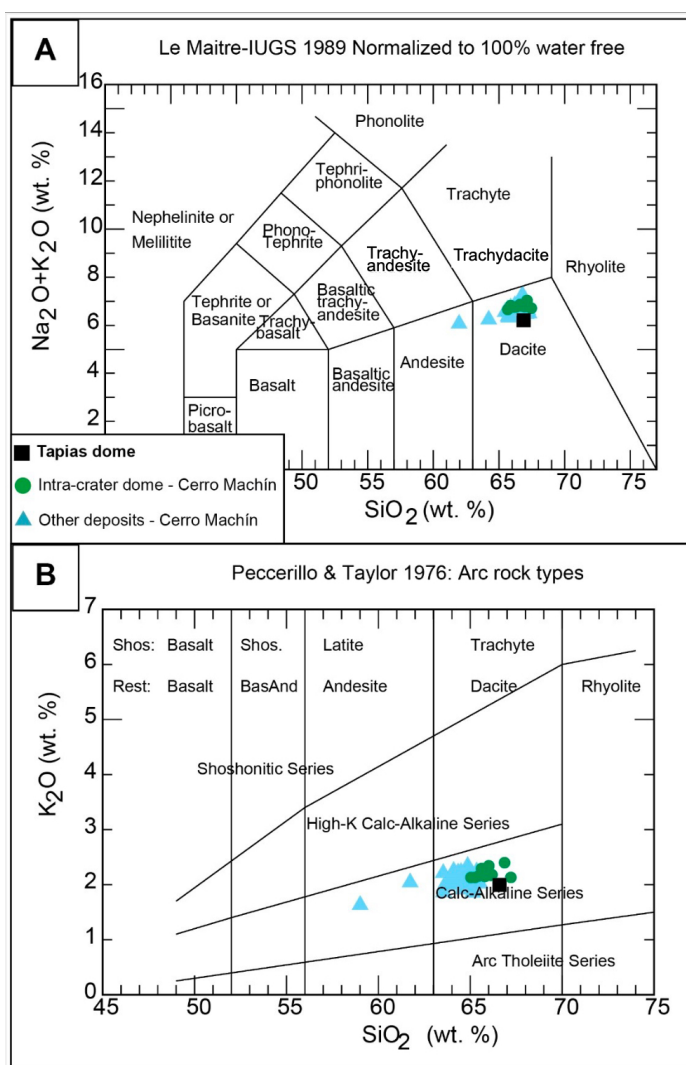
Figure 4. Whole-rock composition of sample MOR17-01 from Tapias (Errázuriz-Henao *et al.*, 2019) dome and Cerro Machín volcano rocks. **A.** TAS diagram. **B.** Arc rock types. Blue triangles refer to data from other deposits of Cerro Machín (Cepeda *et al.*, 1995; Rueda, 2005; Laeger *et al.*, 2013; Regnier, 2015; Errázuriz-Henao *et al.*, 2019).
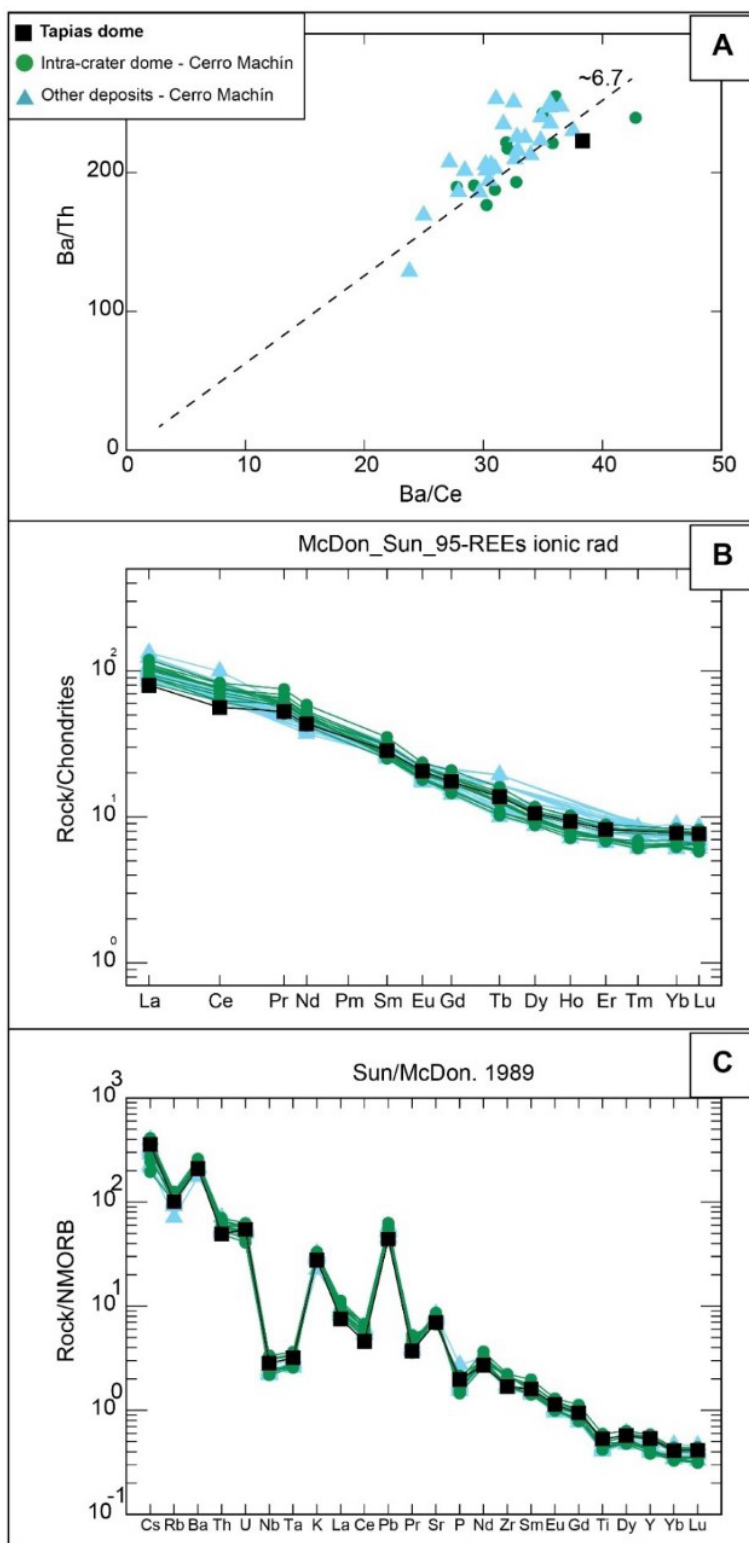
Figure 5. Whole-rock trace element behavior of sample MOR-1701 (Errázuriz-Henao *et al.*, 2019) from Tapias dome and Cerro Machín volcano rocks. **A.** K₂O to Rb ratio. **B.** REE diagram. **C.** Multielement diagram. Blue triangles refer to data from other deposits of Cerro Machín volcano (Rueda, 2005; Laeger *et al.*, 2013; Regnier, 2015; Errázuriz-Henao *et al.*, 2019).
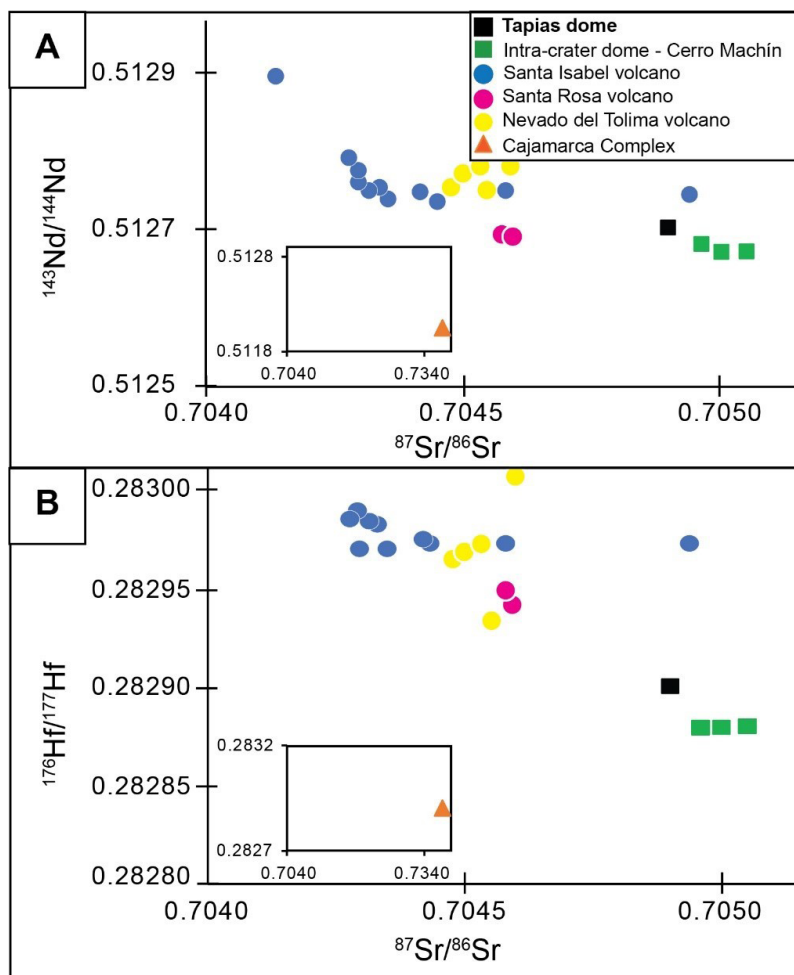
Figure 6. Isotopic compositions for rocks of Tapias dome, compared with Cerro Machín, Santa Isabel (Errázuriz-Henao *et al.*, 2019), Santa Rosa (Cavell, 2020) and Nevado del Tolima (Errázuriz-Henao *et al*., 2021) volcanoes, and the Cajamarca Complex (inset) (Cavell, 2020). **A.** $^{143}Nd/^{144}Nd$ *vs* $^{87}Sr/^{86}Sr$; **B.** $^{176}Hf/^{177}Hf$ *vs* $^{87}Sr/^{86}Sr$.

Geochronology

The K/Ar analysis obtained for the Tapias dome yielded an age of 95 ± 0.05 ka (calculated errors are 2σ). Given that it was obtained from the groundmass, it represents the age for the dome emplacement. This age is ~48 ka older than the Boquerón pyroclastic density current (~47 ka), whose rocks are the product of one of the earliest recognized eruptions of Cerro Machín (Méndez, 2001).

Discussion

Crystallization history and amphibole geothermobarometry of Tapias dome

The textures displayed by the Tapias dome reveal a history of magma fractionation and mixing. The presence and composition of mostly euhedral and large phenocrysts of plagioclase, amphibole, biotite, and quartz, imply a prolonged residence at the magma reservoir, where effective fractionation of mafic phases (*e.g*., olivine, clinopyroxene) permitted the crystallization and growth of minerals with more felsic affinity (Rutherford and Devine, 2003; Holtz *et al*., 2004). The groundmass microlites represent the last crystallization event before or during the eruption (Hammer *et al*., 1999; Cashman and Blundy, 2000). However, disequilibrium features such as plagioclase complex zonation patterns (*e.g.* oscillatory) (Tepley *et al*., 1999) and the inverse zonation of the type II amphiboles, whose rims are enriched in Mg, imply the influx of mafic magma into the magma reservoir and hence magma mixing (Pallister *et al*., 1992; Streck *et al*., 2007).

Given that the two populations of amphibole show equilibrium and disequilibrium features, we use their composition to estimate the conditions of temperature (°C), pressure (GPa), the water content of the melt (wt. % H_2O) (Ridolfi and Renzulli, 2012), and oxygen fugacity (log fO_2) (Ridolfi *et al.*, 2010), at which they crystallized. This allows us to constrain the depths at which amphibole crystallization occurred and hence provide insights into the magma plumbing system. Table 3 shows the data obtained in our geothermobarometric calculations. It is observed that type I amphiboles crystallized between 871 – 875°C, at 0.27 GPa, with water content in the melt of 7.O wt. % H_2O (Figures 7A and 7B), which is similar to the water content from Cerro Machín volcano (Laeger *et al.*, 2013). By assuming a specific gravity of 2.70 g/cm³ for the continental crust (Ridolfi *et al.*, 2010), we determine that type I amphiboles crystallize between 10.2 – 10.4 km (Figure 7C). As shown in the results, the core of the type II amphiboles is like the compositions of the type I amphiboles, hence their crystallization conditions are also similar, with temperatures between 852 and 920°C, at 0.22 – 0.33 GPa and a meltwater content between 6.0 to 7.5 wt. % H_2O (Figure 7B); this suggests that crystallization occurred between 8.9 and 12.3 km (Figure 7C). On the other hand, the rim of type II amphiboles reflects higher crystallization temperatures (880 – 973°C) and lower water contents of the melt (4.2 – 6.6 wt. % H_2O) than their cores, but with similar pressures (0.24 – 0.31 GPa) and hence similar depths (9.1 – 11.8 km) (Figures 7B and 7C). Regarding the oxygen fugacity (Figure 7D), our calculations show similar results for both types of amphiboles, indicating they crystallized in moderate oxidation conditions. These results together with the higher Mg of the rim of the amphibole type II, indicate that it crystallized from a more mafic magma, with relatively lower water content than the one from which the amphibole type I and the core of amphibole type II form. Hence it is assumed that the inverse zonation presented by amphibole type II is the result of the influx of hotter mafic magma into the magma reservoir (8 – 12 km depth) where the residing magma was fractionating (Hawkesworth *et al.*, 2000). This influx of hotter magma is also inferred by 1) the formation of light grey rims on plagioclase pheno- and microphenocrysts, as lighter colors are associated with anorthite-rich compositions (Shcherbakov *et al.*, 2010), and 2) the dissolution features observed in some of the plagioclase crystals that are attributed to the presence of albite rich (XAb >0.6) plagioclase in felsic magmas, as they formed at lower temperatures than the ones required for amphibole crystallization (Rutherford and Devine, 2003; Holtz *et al.*, 2004). Regarding the crystallization of the other mineral phases, Scaillet and Evans (1999) demonstrated that biotite is stable at maximum temperatures of 800°C in water-saturated magma, hence it is possible to assume this as a constrain for the final crystallization temperature for the Tapias dome, as plagioclase and quartz also crystallize at relatively lower temperatures when compare to amphiboles (Scaillet and Evans, 1999; Rutherford and Devine, 2003; Holtz *et al.*, 2004).

Table 3. Estimated crystallization conditions for the amphibole phases identified at Tapias dome.

Code	Type	Ridolfi and Renzulli (2012)			Ridolfi *et al.* (2010)	Leake *et al.* (1997)
		T (°C)	P (GPa)	wt. % H_2O	LogfO_2	Name
C11-b1	I-C	871.4 ±23.5	0.27 ±0.03	7.0 ±1.1	-11.5 ±0.4	Tschermakite
C11-b2	I-C	874.8 ±23.5	0.27 ±0.03	7.0 ±1.1	-11.5 ±0.4	Magnesiohastingsite
C12-a1	II-C	881.1 ±23.5	0.28 ±0.03	7.1 ±1.1	-11.4 ±0.4	Magnesiohastingsite
C12-a3	II-C	920.5 ±23.5	0.33 ±0.04	6.3 ±0.9	-11.4 ±0.4	Magnesiohastingsite
C12-a4	II-C	886.0 ±23.5	0.24 ±0.03	6.0 ±0.9	-11.1 ±0.4	Tschermakite
C12-c0	II-C	864.7 ±23.5	0.24 ±0.03	6.9 ±1.0	-11.5 ±0.4	Magnesiohastingsite
C12-c2	II-C	852.1 ±23.5	0.23 ±0.03	6.9 ±1.0	-11.7 ±0.4	Magnesiohastingsite
C14-a2	II-B	972.8 ±23.5	0.31 ±0.04	4.5 ±0.7	-9.5 ±0.4	Magnesiohastingsite
C14-a4	II-C	870.0 ±23.5	0.28 ±0.03	7.2 ±1.1	-11.6 ±0.4	Tschermakite
C14-a5	II-B	880.2 ±23.5	0.24 ±0.03	6.6 ±1.0	-11.3 ±0.4	Magnesiohastingsite
C14-a7	II-B	951.8 ±23.5	0.29 ±0.03	4.8 ±0.7	-9.6 ±0.4	Tschermakite
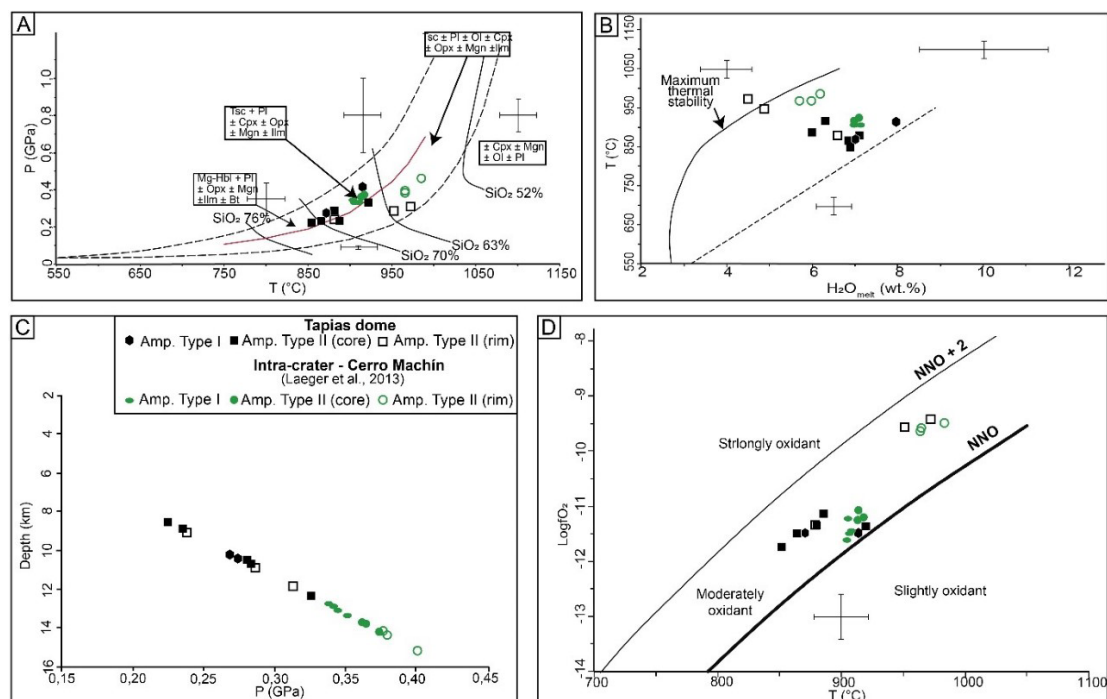
Figure 7. Binary diagrams of geothermobarometric parameters calculated from the Tapias dome and Cerro Machín volcano **A.** Pressure *vs* temperature. **B.** Temperature *vs* water content on the melt. **C.** Depth *vs* pressure. **D.** log fO_2 *vs* temperature. Error bars represent the expected uncertainty from Ridolfi *et al.* (2010). The standard deviation calculated from our data are as follows: T (± 23.5°C), P (± 11.5%), H₂O melt (± 15%), log fO_2 (± 0.4 log units).
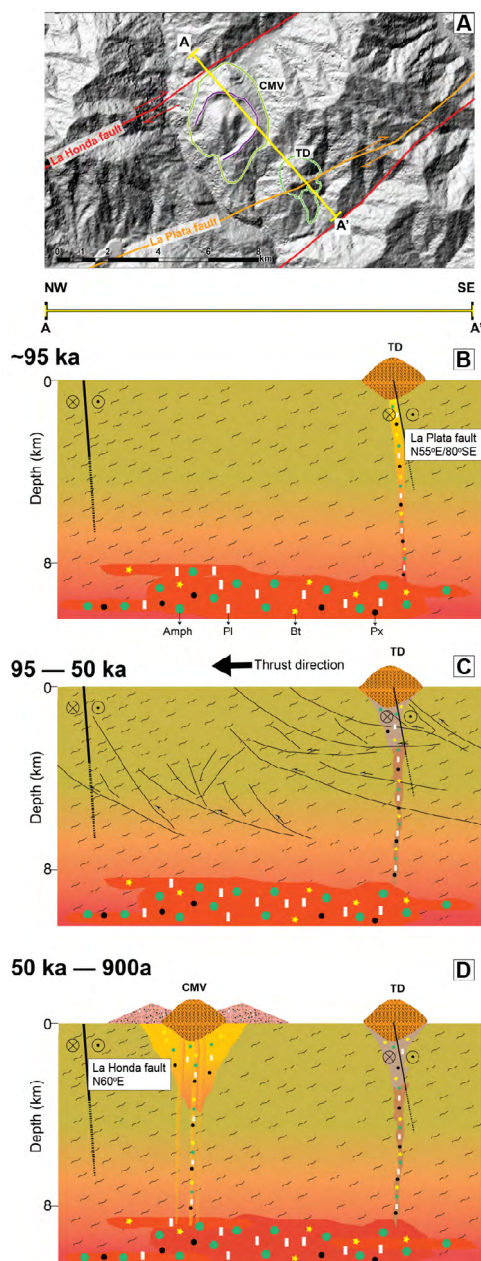
Tapias dome and Cerro Machín volcano

The dacitic composition with a mid-K calc-alkaline affinity of the rocks from both volcanoes, together with the behavior displayed by the REE and multielement diagrams indicate that these magmas are typical of magmas generated by subduction processes that have been residing and evolving in the continental crust (Wilson, 1989). We propose that Tapias dome was fed by the stagnated magma that currently feeds the Cerro Machín; this is supported by their similar isotopic ratios and the ratio of highly incompatible trace elements (Th/Ce), as these do not vary during fractional crystallization or partial melting (Rollinson, 1993). The compositional characteristics of the magmatic source are described in detail by Errázuriz-Henao *et al.* (2021). The persistent dacitic composition (65.04 ± 1.31 wt. %SiO₂) of the products and the presence of the similar mineral assemblage (andesine, calcic amphibole, Mg-rich biotite, and quartz) in products from Cerro Machín and Tapias, are typical of magmas that have been extensively fractionating at the crust, and thus reinforce the hypothesis that both volcanoes were fed by a common magma. The Tapias dome, as the intracrateric Cerro Machín dome, is the result of effusive eruptions likely associated with degassing during magma ascent linked to bubble connection and therefore permeability in an open system (Fink and Anderson, 2000). We infer that the magma stagnation zone is located between ~9 and 15 km depth, based on our calculations for the amphibole crystallization conditions in Tapias dome and the calculations of Laeger *et al.* (2013) for Cerro Machín volcano.

Local tectonics and its relationship with the plumbing system

As discussed above, both Tapias dome and Cerro Machín volcano share a common magma; hence questions arise about their spatial separation (~5 km), the time gap (~50 ka) of the volcanic activity, and why such activity moved from Tapias dome to the area where Cerro Machín is located. We infer that these characteristics occur due to tectonic controls at upper levels of the crust, as the rate and angle of subduction of the Nazca plate have remained fairly constant (60 mm/year) in the last 12 Ma (Gustcher *et al.*, 1999). According to the work performed by Cuéllar-Cárdenas *et al.* (2014) on the Combeima river valley (~8 km NE from Cerro Machín; Figure 8), two structures appear spatially related to the volcanoes studied here; La Plata fault, which can be traced right under the Tapias dome, and La Honda fault, whose trace is observed next to the

NW flank of Cerro Machín volcano. These are synthetic structures from the Otú-Pericos and Ibagué fault systems, respectively (Cuéllar-Cárdenas *et al.*, 2014). Hence, we infer that the deformation created by these systems are the ones controlling the emplacement of the volcanoes. Moreover, these authors also identified three consecutive (although not dated) deformation events: An initial strike-slip cinematic deformation caused by the Otú-Pericos system, followed by the development of thrust folding (in a SEE-NWW direction) due to the propagation of the Otú-Pericos fault, and a final right-lateral transport and clockwise rotation of tectonic blocks, caused by the dextral strike-slip deformation cinematics of the Ibagué fault system. We suspect that these sequences of events are linked to the eruptive events represented by Tapias and Cerro Machín (Figure 8). First, it is possible that the La Plata fault (as part of the Otú-Pericos strike-slip system) acted as a path for magma entrapment and propagation to the surface, allowing the emplacement of Tapias dome (Figure 8B), similar to observed by Le Corvec *et al.* (2013) on analytical experiments. After this, the volcanic activity halted during the period of thrust folding, given the reorganization of the stress (σ_3 orientates vertically) at the crust (Ferrill *et al.*, 2021), inhibiting magma propagation to the surface (Figure 8C) (Valentine and Krogh, 2006; Taherynia *et al.*, 2016). This period of thrust folding is also in agreement with one of the stages of the progressive deformation associated with the development of fold-thrust belts (*e.g.* the SCVTP) proposed by Ferrill *et al.* (2021), where early contractional deformation in the strike-slip regime, presides contractional deformation in a thrust-faulting stress regime. Such type of deformation can occur under local to subregional strike-slip conditions. Hence it is possible that in this area and during this period not only the volcanic activity halted but its locus moved in the SEE-NWW direction (towards the Cerro Machín location), which is the direction of the thrust folding observed by Cuéllar-Cárdenas (2014). Lastly, the deformation caused by the Ibagué fault and its synthetic faults (*e.g.* La Honda fault) caused extensional structures (*e.g. pull-apart*) that allow the emplacement and construction of the Cerro Machín volcano edifice (Figure 8D). Cuéllar-Cárdenas *et al.* (2014) not only identified hydrothermal and sulphur manifestations associated with the Honda fault (at the valley of Combeima river), but also that deformation associated with the Ibagué fault system over imposes the deformation related to the Otú-Pericos fault system. Accordingly, it is considered that the Cerro Machín volcano is located within the deformation zone of the Ibagué fault system and that there is a symbiotic relationship between the fault system and the volcano (Montes *et al.*, 2005; Osorio *et al.*, 2008; Rozo-Gómez, 2012).

Figure 8. Proposed model for the emplacement of Tapias dome and Cerro Machín volcano. **A.** The DEM of the area is added as a geographic reference. **B.** At <95 ka, dike propagation to the surface is aided by the movement of La Plata fault (part of the Otú-Pericos system), allowing the emplacement of Tapias dome. **C.** Between 95 and 50 ka, thrusting deformation in a SE-NW direction inhibits propagation of magma to the surface. **D.** Starting at ~50 ka, extensional deformation caused by the Ibagué fault and its synthetic structures (*i.e.*, La Honda fault), facilitate magma ascent and thus prolonged stagnation and therefore the building of Cerro Machín volcano. Green hexagons represent amphiboles crystallising at the magma chamber (phenocrysts and microphenocrysts) and during ascent (microcrystals), likewise black dots represent biotite, white squares represent plagioclase and yellow starts oxides.

The area where Tapias dome and Cerro Machín volcano are located displays numerous lineaments and faults-like structures (Gómez-Díaz and Mariño-Arias, 2020), however, for some of them there is no consensus regarding their name or even their classification as a fault. For example, *pull-apart* structures have previously been invoked to explain the location of Cerro Machín (Mosquera *et al.*, 1982; Cepeda *et al.*, 1995; Rueda, 2005) and were attributed to deformation caused by the Cajamarca fault. Here we consider that both Cajamarca and La Honda fault are just two different names for the same structure, as their trace seems to follow roughly the same path. However, a discussion of the possible different tectonic faults in the area is beyond the scope of this work. Nevertheless, we consider that our model does explain the coincidence between the sequence of volcanic events and the location of tectonic structures; even if there are no chronological constraints (to the best of our knowledge) for the tectonic deformation events described above so we could establish a direct link.

Conclusions

Tapias dome is a dacitic monogenetic volcano ($<95 \pm 0.05$ ka), characterized by a mineral assemblage of plagioclase (An_{28-48}), amphibole (tschermakite and magnesiohastingsite), biotite, quartz, and Fe-Ti oxides, embedded in a glassy groundmass.

Two amphibole populations are recognized, with and without zonation (High-Mg rims). The core of zoned crystals has the same composition as the unzone ones, indicating an influx of mafic magma into the reservoir.

Geothermobarometric calculations on the amphibole populations in Tapias dome indicates a magmatic stagnation zone at depths between 8.5 and 12.3 km, which would agree with the deepest magma chamber, previously unidentified for the Cerro Machín (10 - 15 km).

Similarities between the rocks of Tapias dome and Cerro Machín volcano suggest that they are fed by the same magma. The rocks are similar in their dacitic composition; their mineral chemistry: andesine plagioclase, Mg-rich biotite, and two populations of amphibole; as well that their isotope ratios (*e.g.*, $^{87}Sr/^{86}Sr$: 0.704907 for Tapias dome and 0.704957 to 0.705046 for Cerro Machín volcano).

The spatiotemporal separation (~50 ka) between Tapias dome and Cerro Machín volcano seems to be controlled by the synthetic faults developed to accommodate the deformation of the Otú-Pericos fault (La Plata fault- Tapias dome), which is later over imposed by the deformation of the Ibagué fault system (La Honda fault – Cerro Machín).

References

Blanco-Quintero, I.F.; García-Casco, A.; Toro, L.M.; Moreno, M.; Ruiz, E.C.; Vinasco, C.J.; Cardona, A.; Lázaro, C.; Morata, D. (2014). Late Jurassic terrane collision in the northwestern margin of Gondwana (Cajamarca Complex, eastern flank of the Central Cordillera, Colombia). *International Geology Review, 56*(15), 1852-1872. https://doi.org/10.1080/00206814.2014.963710

Bohórquez, O.P.; Monsalve, M.L.; Velandia, F.; Gil, F.; Mora, H. (2005). Marco tectónico de la cadena volcánica más septentrional de la Cordillera Central de Colombia. *Boletín de Geología, 27*(1), 55-79.

Cañón-Tapia, E. (2016). Reappraisal of the significance of volcanic fields. *Journal of Volcanology and Geothermal Research, 310,* 26-38. https://doi.org/10.1016/j.jvolgeores.2015.11.010

Cashman, K.; Blundy, J. (2000). Degassing and crystallization of ascending andesite and dacite. *Philosophical Transactions of the Royal Society*

of London. Series A: Mathematical, Physical and Engineering Sciences, 358(1770), 1487-1513. https://doi.org/10.1098/rsta.2000.0600

Cashman, K.V.; Sparks, R.S.J. (2013). How volcanoes work: A 25 year perspective. GSA Bulletin, 125(5-6), 664-690. https://doi.org/10.1130/B30720.1

Cavell, D. (2020). Petrogenesis of Colombian Arc Volcanoes: A regional Study. Ph.D. thesis, University of Birmingham, United Kingdom.

Cepeda, H.; Murcia, L.; Monsalve, M.; Méndez, R.; Núñez, A. (1995). Volcán Cerro Machín, Departamento del Tolima, Colombia: Pasado, presente y futuro. INGEOMINAS, Popayán, Colombia. 48 p.

Connor, C.B.; Conway, F.M. (2000). Basaltic volcanic fields. In: H. Sigurdsson, B. Houghton, S.R. McNutt, H. Rymer, J. Stix (Eds.). Encyclopedia of Volcanoes (pp. 331-343). Academic Press.

Cortés, M.; Angelier, J.; Colletta, B. (2005). Paleostress evolution of the northern Andes (Eastern Cordillera of Colombia): Implications on plate kinematics of the South Caribbean region. Tectonics, 24(1). https://doi.org/10.1029/2003TC001551

Cortés, J. (2022). CFU-PINGU. https://theghub.org/resources/cfupingu

Cuéllar-Cárdenas, M.A.; López-Isaza, J.A.; Carrillo-Lombana, E.J.; Ibáñez-Almeida, D.G.; Sandoval-Ramírez, J.H.; Osorio-Naranjo, J.A. (2014). Control de la actividad tectónica sobre los procesos de erosión remontante: El caso de la cuenca del río Combeima, Cordillera Central de Colombia. Boletín de Geología, 36(1), 37-56.

Diederix, H.; Audemard, F.; Osorio, J.A.; Montes, N.; Velandia, F.; Romero, J. (2006). Modelo morfotectónico de la Falla Transcurrente de Ibagué, Colombia. Revista de la Asociación Geológica Argentina, 61(4), 492-503.

Errázuriz-Henao, C.; Gómez-Tuena, A.; Duque-Trujillo, J.; Weber, M. (2019). The role of subducted sediments in the formation of intermediate mantle-derived magmas from the Northern Colombian Andes. Lithos, 336-337, 151-168. https://doi.org/10.1016/j.lithos.2019.04.007

Errázuriz-Henao, C.; Gómez-Tuena, A.; Parolari, M.; Weber, M. (2021). A biogeochemical imprint of the Panama Basin in the North Andean arc. Geochemistry, Geophysics, Geosystems. 22(7), e2021GC009835. https://doi.org/10.1029/2021GC009835

Ferrill, D.A.; Smart, K.J.; Cawood, A.J.; Morris, A.P. (2021). The fold-thrust belt stress cycle: Superposition of normal, strike-slip, and thrust faulting deformation regimes. Journal of Structural Geology, 148, 104362. https://doi.org/10.1016/j.jsg.2021.104362

Fink, J.H.; Anderson, S.W. (2000). Lava domes and coulees. In: H. Sigurdsson, B. Houghton, S.R. McNutt, H. Rymer, J. Stix (eds.). Encyclopedia of Volcanoes (pp. 307-319). Academic Press.

Foster, M.D. (1960). Interpretation of the composition of trioctahedral micas. U.S Geological Survey Professional Paper, 354(B), 1-49. https://doi.org/10.3133/pp354B

Gómez-Díaz, E.; Mariño-Arias, O.M. (2020). Structural assessment and geochemistry of thermal waters at the Cerro Machin Volcano (Colombia): An approach to understanding the geothermal system. Journal of Volcanology and Geothermal Research, 400, 106910. https://doi.org/10.1016/j.jvolgeores.2020.106910

González, P.D. (2008). Geología de los cuerpos ígneos. In: E.J. Llambías (ed.). Geología de los cuerpos ígneos (pp. 167-195). Universidad Nacional de La Plata - CONICET.

Gudmundsson, A. (2006). How local stresses control magma-chamber ruptures, dyke injections, and eruptions in composite volcanoes. Earth-Science Reviews, 79(1-2), 1-31. https://doi.org/10.1016/j.earscirev.2006.06.006

Gustcher, M.A.; Malavieille, J.; Lallemand, S; Collot, J.Y. (1999). Tectonic segmentation of the North Andean margin: impact of the Carnegie Ridge collison. Earth and Planetary Science Letters, 168(3-4), 255-270. https://doi.org/10.1016/S0012-821X(99)00060-6

Hammer, J.E.; Cashman, K.V.; Hoblitt, R.P.; Newman, S. (1999). Degassing and microlite crystallization during pre-climactic events of

the 1991 eruption of Mt. Pinatubo, Philippines. *Bulletin of Volcanology, 60*(5), 355-380. https://doi.org/10.1007/s004450050238

Hawkesworth, C.J.; Blake, S.; Evans, P.; Hughes, R.; Macdonald, R.; Thomas, L.E.; Turner, S.P.; Zellmer, G. (2000). Time Scales of Crystal Fractionation in Magma Chambers—Integrating Physical, Isotopic and Geochemical Perspectives. *Journal of Petrology, 41*(7), 991-1006. https://doi.org/10.1093/petrology/41.7.991

Holtz, F.; Sato, H.; Lewis, J.; Behrens, H.; Nakada, S. (2004). Experimental Petrology of the 1991-1995 Unzen Dacite, Japan. Part I: Phase Relations, Phase Composition and Pre-eruptive Conditions. *Journal of Petrology, 46*(2), 319-337. https://doi.org/10.1093/petrology/egh077

Janoušek, V.; Farrow, C.M.; Erban, V. (2006). Interpretation of Whole-rock Geochemical Data in Igneous Geochemistry: Introducing Geochemical Data Toolkit (GCDkit). *Journal of Petrology, 47*(6), 1255-1259. https://doi.org/10.1093/petrology/egl013

Jaramillo, J.S.; Cardona, A.; Monsalve, G.; Valencia, V.; León, S. (2019). Petrogenesis of the late Miocene Combia volcanic complex, northwestern Colombian Andes: Tectonic implication of short term and compositionally heterogeneous arc magmatism. *Lithos, 330-331*, 194-210. https://doi.org/10.1016/j.lithos.2019.02.017

Kereszturi, G.; Németh, K. (2012). Monogenetic basaltic volcanoes: genetic classification, growth, geomorphology and degradation. In: K. Németh (ed.). *Updates in Volcanology – New Advances in Understanding Volcanic Systems* (pp. 3-89). InTechOpen. https://doi.org/10.5772/51387

Kim, Y.S.; Peacock, D.C.P.; Sanderson, D.J. (2004). Fault damage zones. *Journal of Structural Geology, 26*(3), 503-517. https://doi.org/10.1016/j.jsg.2003.08.002

Laeger, K.; Halama, R.; Hansteen, T.; Savov, I.P.; Murcia, H.F.; Cortés, G.P.; Garbe-Schönberg, D. (2013). Crystallization conditions and petrogenesis of the lava dome from the ~900 years BP eruption of Cerro Machín Volcano, Colombia. *Journal of South American Earth Sciences, 48*, 193-208. https://doi.org/10.1016/j.jsames.2013.09.009

Le Corvec, N.; Menand, T.; Lindsay, J. (2013). Interaction of ascending magma with pre-existing crustal fractures in monogenetic basaltic volcanism: an experimental approach. *Journal of Geophysical Research: Solid Earth, 118*(3), 968-984. https://doi.org/10.1002/jgrb.50142

Leake, B.E.; Woolley, A.R.; Arps, C.E.; Birch, W.D.; Gilbert, M.C.; Grice, J.D.; Hawthorne, F.C.; Kato, A.; Kisch, H.J.; Krivovichev, V.G.; Linthout, K.; Laird, J.; Mandarino, J.A.; Maresch, W.V.; Nickel, E.H.; Rock, N.M.S.; Schumacher, J.C.; Smith, D.C.; Stephenson, N.C.N.; Ungaretti, L.; Whittaker, E.J.W.; Youshi, G. (1997). Nomenclature of Amphiboles: Report of the Subcommittee on Amphiboles of the International Mineralogical Association Commission on New Minerals and Mineral Names. *Mineralogical Magazine, 61*(405), 295-310. https://doi.org/10.1180/minmag.1997.061.405.13

Maccaferri, F.; Bonafede, M.; Rivalta, E. (2011). A quantitative study of the mechanisms governing dike propagation, dike arrest and sill formation. *Journal of Volcanology and Geothermal Research, 208*(1-2), 39-50. https://doi.org/10.1016/j.jvolgeores.2011.09.001

Martel, S.J. (1997). Effects of cohesive zones on small faults and implications for secondary fracturing and fault trace geometry. *Journal of Structural Geology, 19*(6), 835-847. https://doi.org/10.1016/S0191-8141(97)00002-3

Martínez, L.M.; Valencia, L.G., Ceballos, J.A., Narváez, B.L.; Pulgarin, B.A.; Correa, A.M.; Navarro, S.; Murcia, H.F.; Zuluaga, I.; Rueda, J.B.; Pardo, N. (2014). Geología y Estratigrafía del Complejo Volcánico Nevado del Ruiz. Informe, Servicio Geológico Colombiano.

Maya, M.; Gonzalez, H. (1995). Unidades litodemicas en la Cordillera Central de Colombia. *Boletín Geológico, 35*(2-3), 44-57. https://doi.org/10.32685/0120-1425/bolgeol35.2-3.1995.316

Mejía-Toro, E.L. (2012). Características cinemáticas y condiciones de deformación de un segmento de la Falla Palestina al NE del Volcán Nevado del Ruíz. M.Sc. thesis, Universidad Nacional de Colombia, Bogotá, Colombia.

Méndez-Fajury, R.A. (1989). Catálogo de los volcanes activos en Colombia. *Boletín Geológico, 30*(3), 1-75. https://doi.org/10.32685/0120-1425/bolgeol30.3.1989.165

Méndez, R.A. (2001). Informe sobre la geología y estratigrafía de flujos piroclásticos asociados al volcán Cerro Machín. INGEOMINAS, Manizales. Informe interno, inédito.

Montes, N.; Velandia, F.; Osorio, J.; Audemard, F.; Diederix, H. (2005). Interpretación morfotectónica de la Falla Ibagué para su caracterización paleosismológica. *Boletín de Geología, 27*(1), 95-114.

Mora-Páez, H.; Kellogg, J.N.; Freymueller, J.T.; Mencin, D.; Fernandes, R.M.S.; Diederix, H.; LaFemina, P.; Cardona-Piedrahita, L.; Lizarazo, S.; Peláez-Gaviria, J.R.; Díaz-Mila, F.; Bohórquez-Orozco, O.; Giraldo-Londoño, L.; Corchuelo-Cuervo, Y. (2019). Crustal deformation in the northern Andes – A new GPS velocity field. *Journal of South American Earth Sciences, 89*, 76-91. https://doi.org/10.1016/j.jsames.2018.11.002

Mosquera, D.; Nuñez, A.; Vesga, J. (1982). Mapa Geológico de Ibague (Carta 244, 1:100.000). INGEOMINAS, Bogotá.

Murcia, H.F.; Sheridan, M.F.; Macías, J.L.; Cortés, G.P. (2010). TITAN2D simulations of pyroclastic flows at Cerro Machín Volcano, Colombia: Hazard implications. *Journal of South American Earth Sciences, 29*(2), 161-170. https://doi.org/10.1016/j.jsames.2009.09.005

Murcia, H.; Németh, K. (2020). Effusive Monogenetic Volcanism. In: K. Németh (ed). *Updates in Volcanology* (pp. 1-15). IntechOpen. https://doi.org/10.5772/intechopen.94387

Németh, K.; White, J.D.L.; Reay, A.; Martin, U. (2003). Compositional variation during monogenetic volcano growth and its implications for magma supply to continental volcanic fields. *Journal of the Geological Society, 160*(4), 523-530. https://doi.org/10.1144/0016-764902-131

Németh, K. (2010). Monogenetic volcanic fields: Origin, sedimentary record, and relationship with polygenetic volcanism. In: E. Cañón-Tapia, A. Szakács (eds.). *What Is a Volcano?* (pp. 43-66). Geological Society of America. https://doi.org/10.1130/2010.2470(04)

Osorio, J.; Montes, N.; Velandia, F.; Acosta, J.; Romero, J.; Diederix, H.; Audemard, F.; Núñez, A. (2008). *Paleosismología de la Falla de Ibagué*. INGEOMINAS. https://doi.org/10.32685/9789589789674

Pallister, J.S.; Hoblitt, R.P.; Reyes, A.G. (1992). A basalt trigger for the 1991 eruptions of Pinatubo volcano? *Nature, 356*(6368), 426-428. https://doi.org/10.1038/356426a0

Pansino, S.; Taisne, B. (2019). How Magmatic Storage Regions Attract and Repel Propagating Dikes. *Journal of Geophysical Research: Solid Earth, 124*(1), 274-290. https://doi.org/10.1029/2018JB016311

Paris, G.; Machette, M.; Dart, R.; Haller, K. (2000). Map and database of Quaternary Faults and Folds in Colombia and its Offshore Regions. USGS. Open-File Report 00-0284. https://doi.org/10.3133/ofr00284

Peacock, D.C.P.; Sanderson, D.J. (1996). Effects of propagation rate on displacement variations along faults. *Journal of Structural Geology, 18*(2-3), 311-320. https://doi.org/10.1016/S0191-8141(96)80052-6

Piedrahita, D.A.; Aguilar-Casallas, C.; Arango-Palacio, E.; Murcia, H.; Gómez-Arango, J. (2018). Estratigrafía del cráter y morfología del volcán Cerro Machín, Colombia. *Boletín de Geología, 40*(3), 29-48. https://doi.org/10.18273/revbol.v40n3-2018002

Poveda, E.; Monsalve, G.; Vargas, C.A. (2015). Receiver functions and crustal structure of the northwestern Andean region, Colombia. *Journal of Geophysical Research: Solid Earth, 120*(4), 2408-2425. https://doi.org/10.1002/2014JB011304

Poveda, E.; Julià, J.; Schimmel, M.; Perez-Garcia, N. (2018). Upper and Middle Crustal Velocity Structure of the Colombian Andes From Ambient Noise Tomography: Investigating Subduction-Related Magmatism in the Overriding

Plate. *Journal of Geophysical Research: Solid Earth, 123*(2), 1459-1485. https://doi.org/10.1002/2017JB014688

Rahman, S.; MacKenzie, W.S. (1969). The crystallization of ternary feldspars: a study from natural rocks. *American Journal of Science, 267*, 391-406.

Regnier, A. (2015). Cerro Machin, Colombia: A higly explosive volcano showing signs of unrest. M.Sc. thesis, Université de Genéve, Switzerland.

Ridolfi, F.; Renzulli, A.; Puerini, M. (2010). Stability and chemical equilibrium of amphibole in calc-alkaline magmas: an overview, new thermobarometric formulations and application to subduction-related volcanoes. *Contributions to Mineralogy and Petrology, 160*(1), 45-66. https://doi.org/10.1007/s00410-009-0465-7

Ridolfi, F.; Renzulli, A. (2012). Calcic amphiboles in calc-alkaline and alkaline magmas: thermobarometric and chemometric empirical equations valid up to 1,130°C and 2.2 GPa. *Contributions to Mineralogy and Petrology, 163*(5), 877-895. https://doi.org/10.1007/s00410-011-0704-6

Rollinson, H. (1993). *Using Geochemica Data: Evaluation, Presentation, Interpretation*. Longman, Scientific and Technical. https://doi.org/10.4324/9781315845548

Rozo-Gómez, D.H. (2012). Mecanismos de deformación de la zona de daño de la Falla de Ibague en inmediaciones al volcán Cerro Machín. B.Sc. thesis, Universidad de Caldas, Manizales, Colombia.

Rueda, H. (2005). Erupciones Plinianas del Holoceno en el Volcán Cerro Machín, Colombia. Estratigrafía, Petrografía y Dinámica Eruptiva. M.Sc. thesis, Universidad Nacional Autonoma de México.

Rutherford, M.J.; Devine, J.D. (2003). Magmatic conditions and magma ascent as indicated by hornblende phase equilibria and reactions in the 1995-2002 Soufrière Hills magma. *Journal of Petrology, 44*(8), 1433-1454. https://doi.org/10.1093/petrology/44.8.1433

Scaillet, B.; Evans, B. (1999). The 15 June 1991 Eruption of Mount Pinatubo. I. Phase Equilibria and Pre-eruption P–T–fO$_2$–fH$_2$O Conditions of the Dacite Magma. *Journal of Petrology, 40*(3), 381-411. https://doi.org/10.1093/petroj/40.3.381

Shcherbakov, V.D.; Plechov, P.Y.; Izbekov, P.E.; Shipman, J.S. (2010). Plagioclase zoning as an indicator of magma processes at Bezymianny Volcano, Kamchatka. *Contributions to Mineralogy and Petrology, 162*(1), 83-99. https://doi.org/10.1007/s00410-010-0584-1

Smith, I.E.M.; Németh, K. (2017). Source to surface model of monogenetic volcanism: a critical review. *Geological Society, London, Special Publications, 446*, 1-28. https://doi.org/10.1144/SP446.14

Streck, M.J.; Leeman, W.P.; Chesley, J. (2007). High-magnesian andesite from Mount Shasta: A product of magma mixing and contamination, not a primitive mantle melt. *Geology, 35*(4), 351-354. https://doi.org/10.1130/G23286A.1

Taherynia, M.H.; Fatemi-Aghda, S.M.; Fahimifar, A. (2016). In-Situ Stress State and Tectonic Regime in Different Depths of Earth Crust. *Geotechnical and Geological Engineering, 34*(2), 679-687. https://doi.org/10.1007/s10706-016-9978-9

Tepley, F.J.; Davidson, J.P.; Clynne, M.A. (1999). Magmatic Interactions as Recorded in Plagioclase Phenocrysts of Chaos Crags, Lassen Volcanic Center, California. *Journal of Petrology, 40*(5), 787-806. https://doi.org/10.1093/petroj/40.5.787

Thouret, J.C.; Cantagrel, J.M.; Salinas, R.; Murcia, A. (1990). Quaternary eruptive history of Nevado del Ruiz (Colombia). *Journal of Volcanology and Geothermal Research, 41*(1-4), 225-251. https://doi.org/10.1016/0377-0273(90)90090-3

Thouret, J.C.; Cantagrel, J.M.; Robin, C.; Murica, A.; Salinas, R.; Cepeda, H. (1995). Quaternary eruptive history and hazard-zone model at Nevado del Tolima and Cerro Machin Volcanoes, Colombia. *Journal of Volcanology and Geothermal Research, 66*(1-4), 397-426. https://doi.org/10.1016/0377-0273(94)00073-P

Torres-Orozco, R.; Arce, J.L.; Layer, P.W.; Benowitz, J.A. (2017). The Quaternary history of effusive

volcanism of the Nevado de Toluca area, Central Mexico. *Journal of South American Earth Sciences, 79,* 12-39. https://doi.org/10.1016/j.jsames.2017.07.008

Valentine, G.; Krogh, K. (2006). Emplacement of shallow dikes and sills beneath a small basaltic volcanic center – The role of pre-existing structure (Paiute Ridge, southern Nevada, USA). *Earth and Planetary Science Letters, 246*(3-4), 217-230. https://doi.org/10.1016/j.epsl.2006.04.031

van der Hilst, R.; Mann, P. (1994). Tectonic implications of tomographic images of subducted lithosphere beneath northwestern South America. *Geology, 22*(5), 451-454. https://doi.org/10.1130/0091-7613(1994)022<0451:TIOTIO>2.3.CO;2

van Wyk de Vries, B.; Merle, O. (1998). Extension induced by volcanic loading in regional strike-slip zones. *Geology, 26*(11), 983-986. https://doi.org/10.1130/0091-7613(1998)026<0983:EIBVLI>2.3.CO;2

Vargas, C.; Kammer, A.; Valdes, M.; Rodríguez, C.; Caneva, A.; Sánchez, J.J.; Arias, E.; Cortes, C.; Mora, H. (2005). New Geological and Geophysical Constributions in the Section Ibagué-Armenia, Central Cordillera - Colombia. *Earth Sciences Research Journal, 9*(2), 99-109.

Villagómez, D.; Spikings, R.; Magna, T.; Kammer, A.; Winkler, W.; Beltrán, A. (2011). Geochronology, geochemistry and tectonic evolution of the Western and Central cordilleras of Colombia. *Lithos, 125*(3-4), 875-896. https://doi.org/10.1016/j.lithos.2011.05.003

Wilson, M. (1989). *Igneous Petrogenesis*. Springer. https://doi.org/10.1007/978-94-010-9388-0

Yarce, J.; Monsalve, G.; Becker, T.W.; Cardona, A.; Poveda, E.; Alvira, D.; Ordoñez-Carmona, O. (2014). Seismological observations in Northwestern South America: Evidence for two subduction segments, contrasting crustal thicknesses and upper mantle flow. *Tectonophysics, 637,* 57-67. https://doi.org/10.1016/j.tecto.2014.09.006